Influence of hydrogen on the stress-relaxation properties of 17-4PH martensitic stainless steel manufactured by laser powder bed fusion

N. Guennouni [a,b], D. Maisonnette [b], C. Grosjean [b], E. Andrieu [a], D. Poquillon [a], C. Blanc [a,*]

[a] CIRIMAT, Université de Toulouse, CNRS, INP-ENSIACET, 4 Allée Emile Monso, BP 44362, 31030, Toulouse Cedex 4, France
[b] Pôle MMS, CETIM 7, Rue de La Presse, 42000, Saint-Etienne, France

ARTICLE INFO

Keywords:
A. stress–strain measurements
B. iron alloys
C. plasticity methods
C. surface phenomena
D. phase transformation
D. plasticity

ABSTRACT

To evaluate the interactions between hydrogen and the mechanical behavior of additively manufactured (AM) 17-4PH martensitic stainless steel (MSS), stress-relaxation tests were performed for both non-charged and hydrogen-charged samples. Similar tests were performed for the conventional 17-4PH MSS counterpart (CM). The results clearly indicated significant differences in the relaxation properties between the CM and AM MSSs in the H900 state, which were attributed to the higher reversed austenite amount in the AM MSS than that in the CM MSS. In particular, the influence of hydrogen on the dislocation mobility in the austenite was clearly shown.

1. Introduction

The development of fuel cells has been accompanied by the design of systems comprising metallic structural elements, achievable by additive manufacturing and intended to contain and convey the hydrogen necessary for the fuel cell operation. For safety and security reasons, this technological development should be integrated with road or air transport while adhering to the rigorous in-service criteria. The operating conditions envisaged for the structural elements cover a wide range of temperatures and pressures. High-strength steels can be used, but usually, their mechanical behaviors are sensitive to the presence of hydrogen [1–8]. Two aspects have been widely documented in literature [2–8], namely, hydrogen embrittlement (HE) and the effect of hydrogen on plasticity through hydrogen-dislocation interactions. However, the viscoplasticity enhancement due to hydrogen can be advantageous as it can improve the in-service behavior of structures via stress relaxation near defects resulting from manufacturing steps or in stress concentration areas arising from the geometry of the parts.

The use of high-strength stainless steels, e.g., martensitic stainless steels (MSSs) such as 17-4PH, to manufacture parts with complex shapes by additive manufacturing is currently being considered [7,9–11]. Thus, this study aims to investigate the interactions between hydrogen and the mechanical behavior of additively manufactured (AM) 17-4PH MSS, taking advantage of the fact that this steel exhibits a viscoplastic behavior at room temperature in the absence of hydrogen. Robertson showed that data related to the influence of hydrogen on dislocation mobility can be obtained from stress-relaxation tests [12]. More recently, Ogawa et al. [13] revealed the influence of hydrogen-dislocation interactions on the mechanical behavior of hydrogen-containing Fe–24Cr–19Ni-based austenitic stainless steel by performing stress-relaxation tests. Therefore, in this study, the viscoplastic behavior of hydrogen-charged 17-4PH MSS was analyzed based on incremental stress-relaxation tests at room temperature to evaluate the effect of hydrogen on the relaxation behavior of MSS. The tests were carried out on cathodically hydrogen-charged specimens by comparison with non-charged samples. The mechanical responses of AM 17-4PH MSS and its conventionally manufactured (CM) counterpart were compared to determine the influence of the additive manufacturing process on the relaxation behavior of the 17-4PH MSS and identify the microstructural elements controlling the relaxation behavior. Both MSSs were studied in the same heat treatment state, i.e., the H900 state. The microstructural differences between the AM and CM 17-4PH MSSs studied here are already described in our previous papers [14–16]; thus, only the main results are presented in the experimental section (materials). Primarily, the AM MSS contains much more reversed austenite than the CM MSS [16]. In this study, particular attention is given to the role of reversed austenite in the relaxation behavior of the AM 17-4PH MSS.

* Corresponding author.
E-mail address: christine.blanc@ensiacet.fr (C. Blanc).

https://doi.org/10.1016/j.msea.2021.142125

2. Experimental

2.1. Materials and samples

The material studied was 17-4PH MSS manufactured by laser powder bed fusion (L-PBF), referred to as AM. Its chemical composition is presented in Table 1. All AM parts were built under Ar using an EOS DMLS M290 machine featuring a 400 W laser. The building parameters were fixed as follows: building plate maintained at 200 °C, a 67° rotation between each layer, and a 40 μm layer thickness. The built parts were 100 mm × 15 mm × 70 mm parallelepipeds, with the building direction relative to the 70 mm side, and cylinders (15 mm in diameter and 70 mm in height) with the cylinder axis parallel to the building direction. Cylindrical samples of CM 17-4PH MSS with a 15 mm diameter were extracted from a 50 mm diameter wrought cylinder in the H1025 metallurgical state. They have a similar composition (Table 1) to the AM samples and are referred to as CM.

For both the AM and CM MSSs, microstructural characterization and hydrogen content measurements were performed on small coupons extracted from the AM parallelepipeds and CM cylinders, respectively. Axisymmetric tensile specimens were machined to 4 mm diameter and 30 mm gauge length from the 15 mm diameter cylinders of the AM and CM MSSs.

All the AM and CM samples were subjected to the conventional H900 heat treatment (annealing step at 1040 °C for 30 min, air quenching, and aging treatment at 482 °C for 1 h). A previous study was devoted to the microstructural characterization of both AM and CM MSSs [16]. The austenite content was evaluated using energy-dispersive X-ray diffraction (XRD) analyses through iterative peak simulations. Only the main results from Ref. [16] are provided here, as illustrated in Fig. 1. The CM-H900 MSS has a fully martensitic microstructure (0.8 ± 0.2% of austenite) with martensite lath widths between 700 nm and 2.5 μm. Scanning transmission electron microscopy (STEM, not shown here) indicated numerous NbC precipitates (mean diameter of 0.13 ± 0.01 μm) and Cu-rich precipitates of approximately 4 nm in diameter. The AM-H900 samples contained 12.6 ± 0.3% of austenite. The austenite content was 12.5 ± 0.3% in the as-built parts, but it was not detected after solution heat treatment. STEM energy-dispersive spectroscopy maps of Ni showed that the main component of the austenite in the AM-H900 sample was reversed austenite. Such a large amount of reversed austenite was due to the heterogeneous distribution of austenite-stabilizing alloying elements and to the finer martensite lath sizes (widths between 50 and 800 nm), promoting both austenite nucleation and growth. Furthermore, the AM-H900 samples contained three times less numerous and thinner NbC precipitates (mean diameter of 0.10 ± 0.01 μm) and larger Cu precipitates (diameters varying from 10 to 15 nm) than CM-H900. Furthermore, STEM observations showed no difference in the dislocation density between the two MSSs. The annealing treatment at 1040 °C probably explains the low dislocation density in the AM-H900 samples.

2.2. Experimental methods and techniques

2.2.1. Hydrogen charging and measurement of hydrogen content

Small coupons (15 mm × 3 mm × 2 mm) and cylindrical tensile specimens were cathodically hydrogen-charged in a 10^{-3} M H_2SO_4 solution under a constant current density of 10 mA cm^{-2} for a given duration (24, 72, 144, and 288 h). Before charging, the sample surface was abraded from P600 to P2400 grade using SiC paper and then polished from 6 μm to 0.25 μm grit using diamond paste. Concerning the tensile specimens, a silicon coating was applied on the sample, except for the gauge length. The hydrogen content was measured using a Bruker G8 GALILEO Instrumental Gas Analyzer for the small coupons to evaluate the hydrogen content introduced because of the cathodic charging and for the tensile specimens (by using one half of a sample) after the mechanical tests. The measurements were repeated at least three times.

The hydrogen diffusion in the cylindrical specimens was numerically simulated using Fick's first law. A two-dimensional axisymmetric finite element model (FEM [17]) was used to evaluate the hydrogen gradient through the sample under different boundary conditions. Quadratic isoparametric finite elements were used and axial symmetry was considered to limit the mesh size. Two values of the apparent hydrogen diffusion coefficient D_{app} were used, i.e., 10^{-8} and 10^{-9} cm^2 s^{-1}, based on both experimental results (see section 3) and literature data [18] by considering a mainly martensitic microstructure with hydrogen diffusion in martensite easier than hydrogen diffusion in austenite [19–21]. For the non-charged samples, the hydrogen content was estimated to be between 1.5 and 2 ppm for both MSSs, so that the initial hydrogen concentration C_0 was fixed at 1.5 ppm (wt.). The hydrogen concentration at the surface during cathodic charging was denoted as C_1. Different values were tested from C_1 10^3C_0 to C_1 10^6C_0 because a precise hydrogen concentration on the surface exposed to the H_2SO_4 solution cannot be obtained. The relative increment in the hydrogen content was defined as $(C–C_1)/(C_0–C_1)$, where C is the local hydrogen content. In the range tested, the boundary conditions did not significantly change the value of the relative increment in hydrogen content as long as C_1 was much higher than C_0.

2.2.2. Mechanical tests

Tensile and incremental stress-relaxation tests were performed using the tensile specimens described in section 2.1. Both tests were performed in air at room temperature (controlled at 25 ± 1 °C) for the non-charged and hydrogen-charged samples. The interval between the end of the hydrogen charging and the beginning of the mechanical tests was less than 1 h.

The tensile tests were performed using an MTS machine with a 30 kN force cell and an extensometer with a gauge length of 25 mm. They were carried out up to fracture at a 10^{-3} s^{-1} strain rate. At the end of each test, the diameter of the specimen was measured using a Keyence CV-H500C camera, all along the gauge length at different distances from the fracture surface. The strain ε_f and stress σ_f to fracture were calculated by measuring the minimum section at necking and applying the assumption of volume conservation during plastic deformation.

The incremental stress-relaxation tests were performed as depicted in Fig. 2. The tests involved successive loading steps for incremental stress levels, with a strain-holding step interposed between two loading steps. The specimens were first strained to a stress level equal to 80% of the yield stress $YS_{0.2}$ using a strain rate of 10^{-3} s^{-1}; then, the total strain was held for 10 min, with the extensometer value as the reference strain. During this period, the decrease in stress was continuously recorded at a 20 Hz frequency. At the end of the 10 min relaxation period, the

Table 1
Chemical composition of the AM and CM MSSs (wt.%; in ppm for N and O).

	C	Mn	Si	S	P	Ni	Cr	Mo	Cu	Nb	N (ppm wt.)	O (ppm wt.)	Fe
CM-H900	**0.036** ± *0.002*	**0.39** ± *0.01*	**0.35** ± *0.02*	≤ **0.005**	**0.016** ± *0.003*	**4.49** ± *0.11*	**15.42** ± *0.19*	**0.15** ± *0.01*	**3.24** ± *0.10*	**0.26** ± *0.02*	**140** ± **2**	< **2**	**Bal.**
AM-H900	**0.028** ± *0.002*	**0.32** ± *0.01*	**0.71** ± *0.03*	≤ **0.005**	**0.007** ± *0.002*	**4.08** ± *0.10*	**16.20** ± *0.19*	≤ **0.020**	**3.56** ± *0.11*	**0.27** ± *0.02*	**310** ± *6*	< **2**	**Bal.**

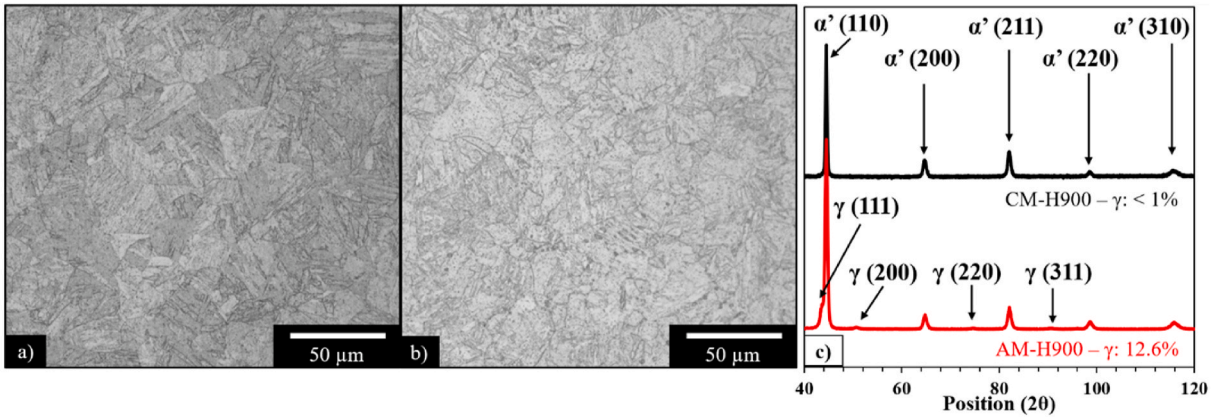

Fig. 1. Observations using an Axiover A1m Zeiss optical microscope, after chemical etching of the a) CM-H900 and b) AM-H900 samples. c) Experimental X-ray diffractograms obtained using a Bruker D8 GIXRD machine with a Cu anticathode for the AM-H900 and CM-H900 samples. (Color online only; two columns). (For interpretation of the references to colour in this figure legend, the reader is referred to the Web version of this article.)

specimen was unloaded until 300 MPa and then reloaded at a higher stress level. The cycle was repeated by incrementing the stress level with increasing steps of 10% $YS_{0.2}$ until fracture of the specimen. For both the non-charged and hydrogen-charged specimens, the $YS_{0.2}$ value was the value measured for the non-charged specimens, i.e., 1255 ± 5 MPa and 1288 ± 7 MPa for CM-H900 and AM-H900, respectively. In section 3, the true value of the stress is specified considering the influence of hydrogen on the MSS mechanical properties, particularly on the $YS_{0.2}$ values. Despite an optimized control of the displacement, the first relaxation step at a stress level of 80% $YS_{0.2}$ was not used for quantitative analyses. This led to relaxation curves (Fig. 3) in which two regimes could be distinguished. During the variable-rate relaxation (VRR) regime, the decrease in stress is very rapid, whereas it is gradual with an approximately steady rate during the steady-rate relaxation (S_tRR) regime [22]. In Fig. 3, σ_0 is the initial relaxation stress, and σ_∞ is the stress at the end of the relaxation period. The transition between these two regimes occurs at a threshold stress σ_t, defined as

$$\sigma_t \quad \sigma_0 \quad 0.9\,(\sigma_0 \quad \sigma_\infty) \qquad \text{Equation 1}$$

σ_t is associated with critical time t_R. The stress-relaxation ability (SRA) is then defined as

$$SRA \quad \frac{\sigma_0 \quad \sigma_t}{\sigma_0} \qquad \text{Equation 2}$$

The average stress-relaxation rate (SRR) in the VRR regime was calculated as

$$SRR \quad \frac{\sigma_0 \quad \sigma_t}{t_R} \qquad \text{Equation 3}$$

Finally, to further understand the hydrogen-dislocation interactions, an interrupted stress-relaxation test protocol, similar to the protocol defined above, was developed. The only difference was that after the first relaxation cycle (specimen strained to 80% $YS_{0.2}$, relaxation step for 10 min, and then unloading to 300 MPa), the specimen was maintained at a constant load of 300 MPa for 1 week, i.e., 168 h, before being subjected to the end of the relaxation test.

All mechanical tests were repeated three times for each condition to ensure reproducibility. In the following, only one representative curve is given for each condition. After each test, the fracture surface was observed using an FEI Quanta 450 scanning electron microscope (SEM). Post-mortem energy-dispersive XRD analyses were performed on the fractured specimens, both at the fracture surfaces and 1.5 cm away from the fracture surfaces, to determine the austenite to martensite ratio. The apparatus, developed by CETIM, was equipped with a W anticathode that emits a polychromatic white X-ray beam. The energy range was 12–40 keV, and the energy-dispersive detector corresponded to an angle of 18.25°.

3. Results

3.1. Hydrogen global content and distribution

Fig. 4a shows the hydrogen contents measured for both the AM and CM samples for hydrogen-charging durations of 0–288 h. For both MSSs, the hydrogen content slightly increased after 24 h of hydrogen charging, leading to a similar hydrogen content (~3 ppm). Then, it increased more rapidly, with the hydrogen content of the AM samples always higher than that of the CM samples for a given hydrogen-charging duration.

The results suggested significant differences in the hydrogen-microstructure interactions between the two MSSs, including both diffusion and trapping phenomena. The influence of pores in the AM samples could not be disregarded, even though the porosity was estimated to be lower than 0.1% (Archimedes porosity measurements). Literature data clearly showed that austenite has a higher hydrogen solubility than martensite, and hydrogen diffusion is easier in martensite [3,19–21,23]. Therefore, the differences in the austenite content between the two MSSs (0.8% and 12% for the CM and AM samples, respectively) were expected to lead to different hydrogen profiles, with higher hydrogen contents in the AM samples [23]. Furthermore, the differences in the size and distribution of NbCs and Cu precipitates could also contribute to explaining the results. Indeed, these precipitates and/or their interfaces with the matrix are also identified as potential hydrogen-trapping sites [5,24], even though NbCs are likely not to be efficient trapping sites for both MSSs considering their mean size [5,25].

In literature, the values of D_{app} vary in a large range, from 10^{-12} cm^2 s^{-1} for austenitic stainless steel, e.g., 304 SS [20], to 10^{-7} cm^2 s^{-1} for a martensitic structure [18]. As explained in section 2, the radial profiles of hydrogen concentration for different values of D_{app}, i.e., 10^{-9} cm^2 s^{-1} and 10^{-8} cm^2 s^{-1} in Fig. 5a and b, respectively, were obtained from FEM. These values were chosen because of the good agreement between the experimental hydrogen contents, as presented in Fig. 4a, and the simulated profiles (Fig. 5). For a better comparison, the relative hydrogen increase corresponding to the hydrogen-charging durations chosen in the present work was calculated using the simulated profiles with the two values of D_{app} (Fig. 4b). The results clearly showed that the experimental data for the CM samples were in good agreement with the D_{app} value of 10^{-9} cm^2 s^{-1}, whereas the D_{app} value of 10^{-8} cm^2 s^{-1} was more relevant for the AM samples. In addition to the previous comments concerning the hydrogen solubility and diffusivity in both austenitic and martensitic structures, the presence of a large amount of austenite/-martensite interfaces in the AM samples, as well as the smaller lath size, was assumed to explain this difference [21,23]. However, it should be

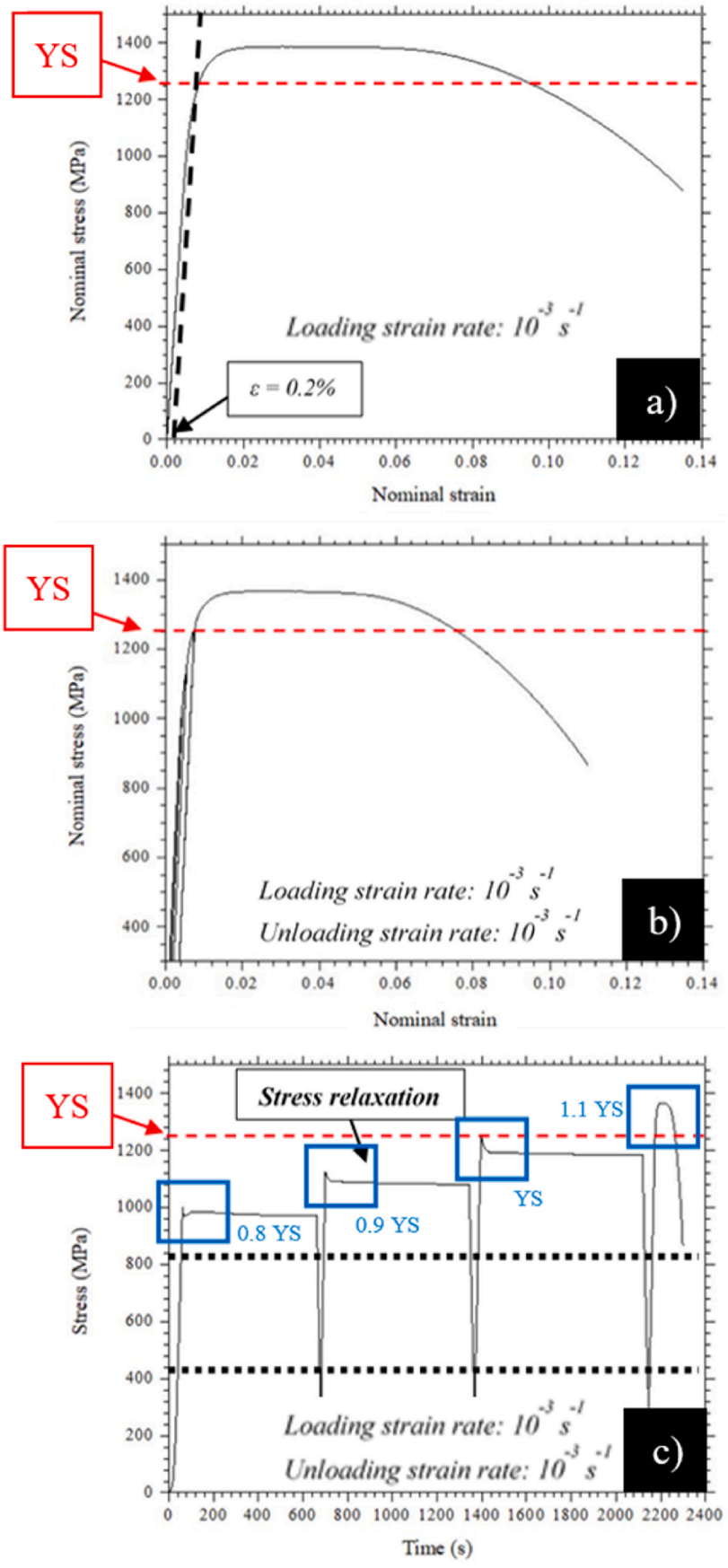

Fig. 2. Methodology used for the incremental stress-relaxation tests: a) tensile test to determine $YS_{0.2}$, b) nominal stress vs. nominal strain curve during tensile test with incremental relaxation steps, and c) stress vs. time curve plotted during a relaxation test. Each step includes a mechanical loading step at a strain rate of 10^{-3} s^{-1}, a 10 min relaxation step, and a mechanical unloading at the same strain rate. The initial stress values used for incremental relaxations are proportional to $YS_{0.2}$, which is determined as shown in a). (Color online only). (For interpretation of the references to colour in this figure legend, the reader is referred to the Web version of this article.)

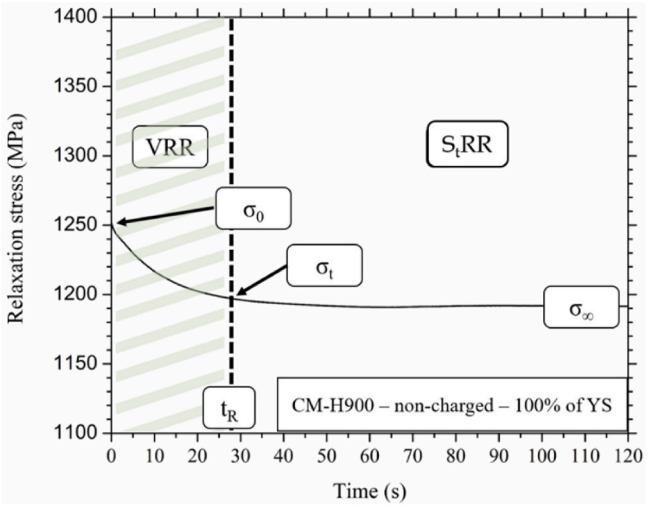

Fig. 3. Schematic of a relaxation curve. VRR and S_tRR regimes are identified using the threshold stress σ_t given by Equation (1) and the critical time t_R [21]. σ_0 is the initial relaxation stress, and σ_∞ is the stress at the end of the relaxation period. (Color online only).

noted that under the hydrogen-charging conditions used, the steady state was not reached. Calculations of the relative hydrogen increase for long charging durations (Fig. 4b) indicated that a 1440 h charging period would be necessary for the AM samples to saturate, but would not lead to saturation for the CM samples. Therefore, for the mechanical tests, it is necessary to consider that for both MSSs, the hydrogen content is not homogeneous in the cylindrical specimens, and the hydrogen profiles are likely to differ between the two MSSs even for a similar global hydrogen content. The FEM profiles were also calculated by considering a desorption step (4, 24, and 168 h), as illustrated in Fig. 5. The profiles obtained after 4 h and 24 h desorption periods (Fig. 5) showed that hydrogen desorption could be neglected for all mechanical tests except the interrupted stress-relaxation tests with a 168 h desorption step.

3.2. *Influence of hydrogen on tensile properties*

Fig. 6 displays the tensile curves plotted for the non-charged and hydrogen-charged samples at three hydrogen-charging durations, i.e., 24, 72, and 144 h, for both the AM and CM samples.

For the non-charged specimens, no significant difference was observed between the CM and AM samples with respect to the $YS_{0.2}$ and flow stress values. Nevertheless, necking began at a higher strain for the CM sample. Moreover, the fracture occurred at a final diameter significantly lower than that of the AM samples (Table 2), which resulted in higher circumferential stresses linked to the increase in stress triaxiality due to the notch effect (necking). Therefore, radial cracks were found for the CM samples on the fracture surfaces where necking was clearly observed (Fig. 7a), whereas they were less visible for the AM samples (Fig. 7e). For both samples, a cup and cone global fracture surface with a ductile fracture mode having dimples was observed. Post-mortem energy-dispersive XRD analyses of the fractured specimens showed that the CM samples contained no austenite on both the fracture surfaces and 1.5 cm away from the fracture surfaces. For the AM samples, there was no austenite on the fracture surfaces, but 1.2 ± 0.4% austenite was found 1.5 cm away from the fracture surfaces compared to 12% austenite in the initial microstructure. These results highlighted the transformation of austenite into martensite, known as the TRIP effect [23,26], which requires sufficient plastic deformation to be activated, as in the necking zone. The TRIP effect should explain, in addition to the pores [16], the reduced ductility of the AM samples, as manifested by the lower strain to fracture values (Table 2).

Fig. 6 also indicates that for the CM samples, the tensile curves plotted for the hydrogen-charged samples are similar to those plotted for the non-charged samples as long as the strain remains uniform. When necking began to be observed, the hydrogen-charged samples promoted strain localization, which could be related to the influence of hydrogen on the strain-rate sensitivity. However, this did not lead to a major decrease in the strain to fracture (Table 2). For the AM samples, a similar behavior was observed for the 24 h hydrogen-charging duration, i.e., a hydrogen content globally similar to that measured for CM samples under the same hydrogen-charging duration. Nevertheless, the influence of hydrogen on the strain-rate sensitivity seemed to be lower for the AM samples than for the CM samples. For longer hydrogen-charging durations, which led to significantly higher hydrogen contents in the AM samples than in the CM samples (Fig. 4), the $YS_{0.2}$ and flow stress were observed to decrease significantly for the AM samples, which suggested that hydrogen promoted the dislocation mobility of these samples [2,12,27–32]. This could be attributed to the relaxation of internal stresses, either during hydrogen charging or during the tensile test. Considering the differences in behavior between the CM and AM samples, hydrogen was suspected to primarily modify the mobility of dislocations in austenite [33], even though the differences in hydrogen content and distribution between the two MSSs could not be neglected. Furthermore,

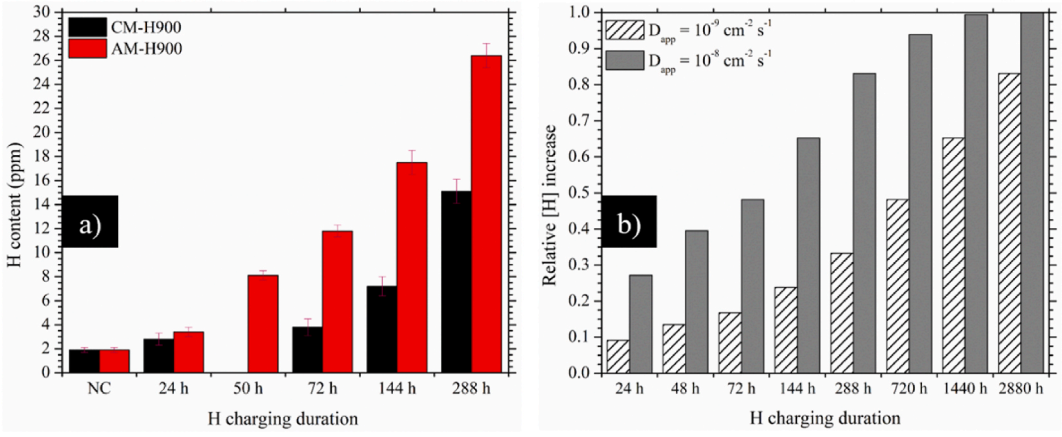

Fig. 4. a) Hydrogen contents of the CM and AM 17-4PH MSSs depending on the hydrogen-charging condition. Hydrogen contents of the non-charged (NC) samples are also indicated as reference values for both MSSs. As a comparison, b) shows the relative increment in hydrogen content determined from the simulated hydrogen profiles shown in Fig. 5, as detailed in the text. (Color online only). (For interpretation of the references to colour in this figure legend, the reader is referred to the Web version of this article.)

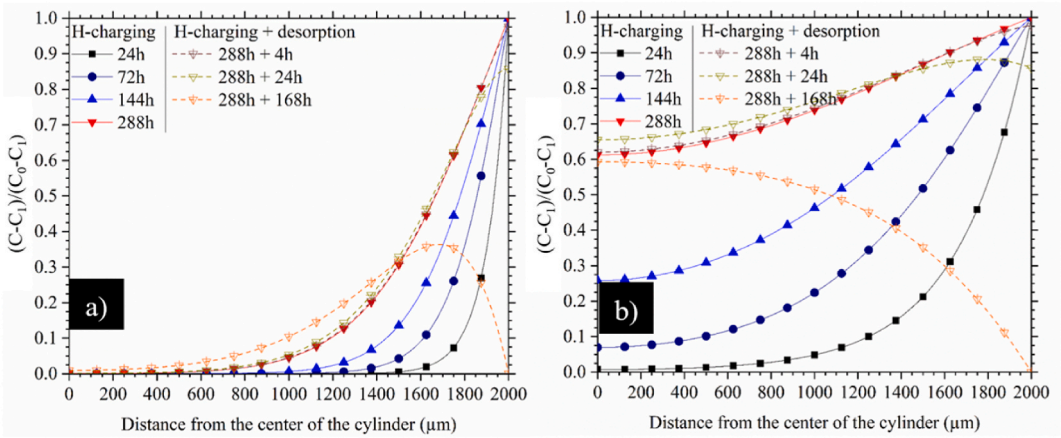

Fig. 5. FEM simulated hydrogen-diffusion profiles for an apparent hydrogen-diffusion coefficient of a) $D_{app} = 10^{-9}$ cm^2 s^{-1} and b) $D_{app} = 10^{-8}$ cm^2 s^{-1}. The simulation conditions are detailed in the experimental section. The hydrogen profiles are for four hydrogen-charging durations, i.e., 24, 72, 144, and 288 h. For the 288 h hydrogen charging, the simulated hydrogen-diffusion profiles after 4, 24, and 168 h desorption periods are also plotted. (Color online only). (For interpretation of the references to colour in this figure legend, the reader is referred to the Web version of this article.)

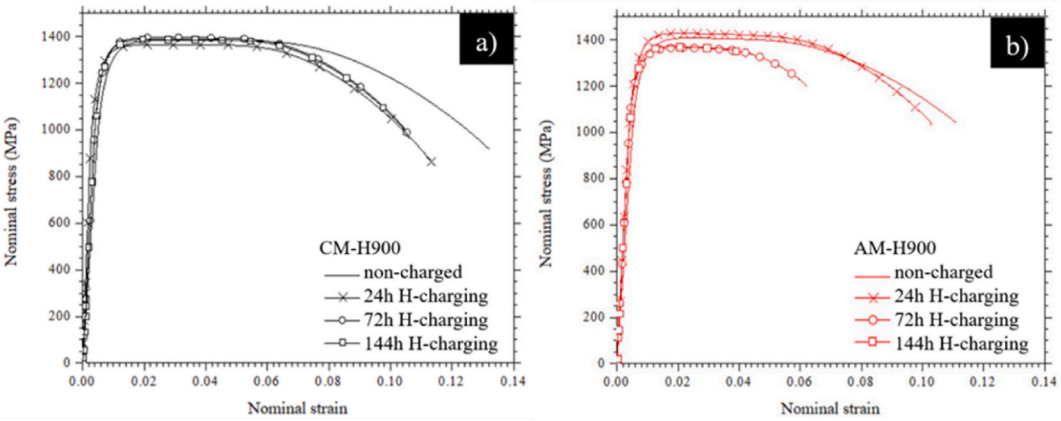

Fig. 6. Tensile curves for the a) CM and b) AM samples at different hydrogen-charging durations. The tensile curves plotted for the non-charged samples are also indicated for comparison. (Color online only). (For interpretation of the references to colour in this figure legend, the reader is referred to the Web version of this article.)

Table 2
Final diameters measured on the tensile specimens after the tensile tests as well as strain to fracture and stress to fracture values calculated from those data. All values are given for both the non-charged and hydrogen-charged (H-charged) samples at different hydrogen-charging conditions.

	Sample	Final diameter (mm)		Strain to fracture		Stress to fracture (MPa)	
		CM	AM	CM	AM	CM	AM
H non-charged	1	2.48	2.83	0.96	0.68	2244	1941
	2	2.47	2.85	0.97	0.67	2273	1930
	3	2.49	2.91	0.94	0.64	2228	1937
24 h H-charging	1	2.59	2.92	0.87	0.63	2172	1930
	2	2.57	2.93	0.88	0.62	2163	1937
	3	2.57	2.90	0.88	0.64	2162	1931
72 h H-charging	1	2.69	3.46	0.79	0.29	2078	1606
	2	2.71	3.48	0.78	0.28	2068	1608
	3	2.71	3.46	0.78	0.29	2067	1605
144 h H-charging	1	2.89	3.96	0.65	0.03	1812	1386
	2	2.91	3.95	0.64	0.03	1815	1385
	3	2.90	3.95	0.64	0.03	1809	1383

for the AM samples, the strain value at which necking started was found to decrease when the hydrogen content increased. Subsequent possibilities for the development of plastic strain after necking also seemed to be decreased for the AM samples, and even reduced to zero in the 144 h hydrogen-charging duration for which necking was not observed (Table 2). Compared with the non-charged AM samples, the strain to fracture was reduced by 57% and 95% for the 72 h and 144 h hydrogen-charged AM samples, respectively (Table 2) [3,8,33]. The behavior of the AM samples after necking might also be explained, at least partially, by considering the transformation of reversed austenite into martensite, as indicated previously for the non-charged samples, with the hypothesis that hydrogen could affect the stability of the reversed austenite, as shown by Wang et al. [34] and Maksimovich et al. [35].

The fracture surfaces observed after the tensile tests (Fig. 7) showed a ductile fracture mode for all the hydrogen-charged CM samples. Radial cracks were clearly observed for all samples, except for that corresponding to the 144 h hydrogen-charging duration (Fig. 7d), in which necking was reduced (Table 2) so that the stress to fracture was not high enough to generate radial cracks. This highlighted the onset of hydrogen-induced damage associated with the increase in hydrogen content compared to the shorter charging durations, which is in agreement with the observations of some zones with intergranular and cleavage fracture modes. For the 24 h hydrogen-charged AM sample

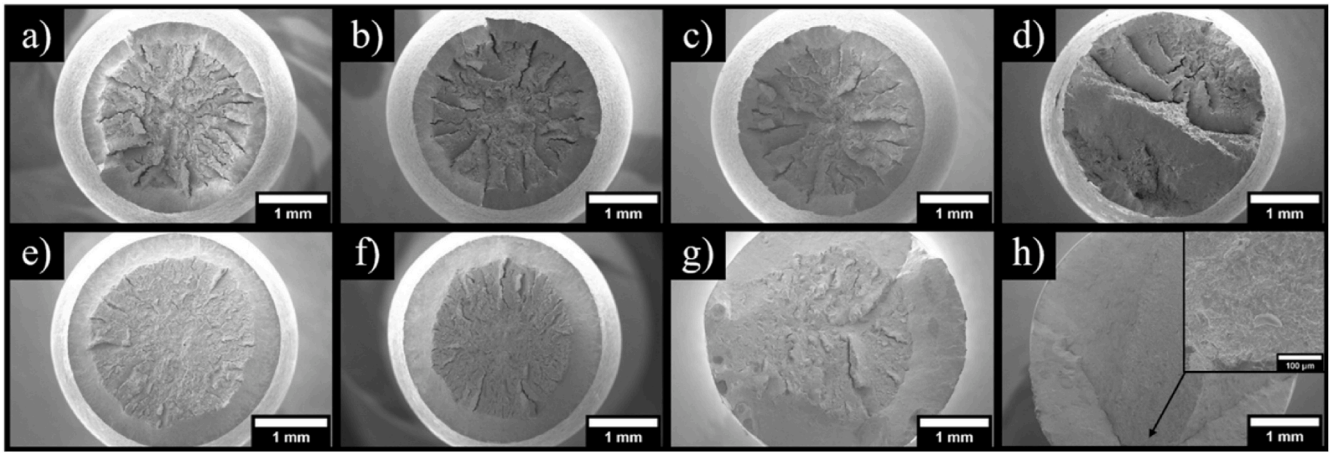

Fig. 7. SEM observations of fracture surfaces for both the (a, b, c, and d) CM and (e, f, g, and h) AM samples at different hydrogen-charging conditions: (a and e) non-charged, (b and f) 24 h hydrogen-charging, (c and g) 72 h hydrogen-charging, and (d and h) 144 h hydrogen-charging. (Color online only).

(Fig. 7f), the fracture surface was similar to those of the non-charged AM sample and the 24 h hydrogen-charged CM sample, which could be explained, at least partially, by the globally similar hydrogen content and distribution. On the contrary, for longer charging durations, which led to significantly higher hydrogen contents of the AM samples than those of the CM samples, necking was strongly reduced and even nonexistent for the 72 h and 144 h hydrogen-charging conditions, respectively, which is in agreement with the tensile curves. A 300 µm wide cleavage zone was observed for the 144 h hydrogen-charged samples near the specimen edge, and some cracks with intergranular fracture mode were observed on the specimen surface. Therefore, the fracture surfaces observed for the AM samples showed the onset of hydrogen-induced damage [8,29,36] for shorter charging durations compared to the CM samples.

3.3. Stress-relaxation properties of 17-4PH MSS: influence of hydrogen

3.3.1. Analysis of the stress-relaxation curves for non-charged samples

The stress-relaxation curves plotted for the non-charged samples (Fig. 8) indicated that the decay of stress that occurred during the strain-holding step was slightly lower for the AM samples than for the CM samples, particularly during the first relaxation step (90% $YS_{0.2}$). However, for both materials, the relaxation stress σ_∞ increased when switching from one relaxation step to the following one, which was likely due to a strain-hardening component. Furthermore, for both MSSs, the stress-relaxation amplitude increased when the initial stress level was increased, with an increase in the SRA values (Fig. 9a and b). This could be related to an increase in the density of mobile dislocations [37], even though the total dislocation density should be considered almost constant owing to the slight increase in plastic strain between

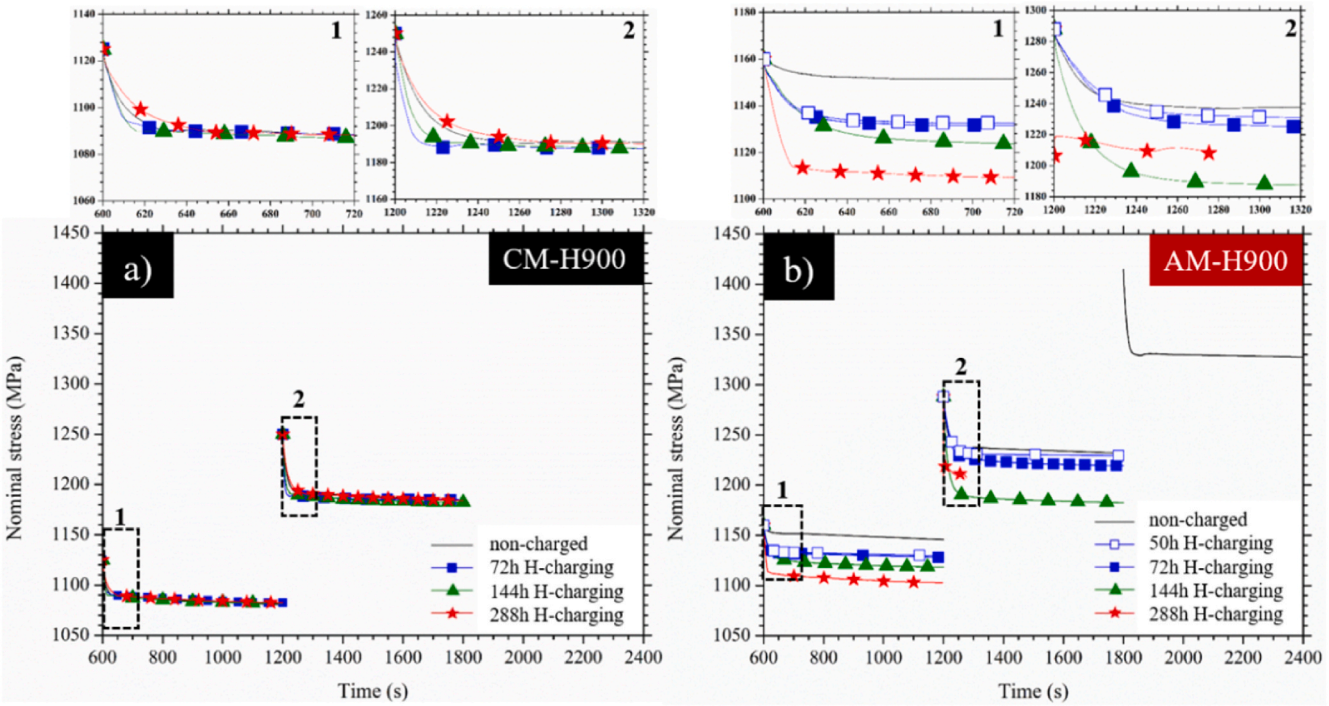

Fig. 8. Stress-relaxation curves in the nominal stress vs time representation for the a) CM and b) AM samples, for both the non-charged and hydrogen-charged samples at different hydrogen-charging durations. Inserts indicate zoomed views of the first 120 s of the relaxation steps. (Color online only). (For interpretation of the references to colour in this figure legend, the reader is referred to the Web version of this article.)

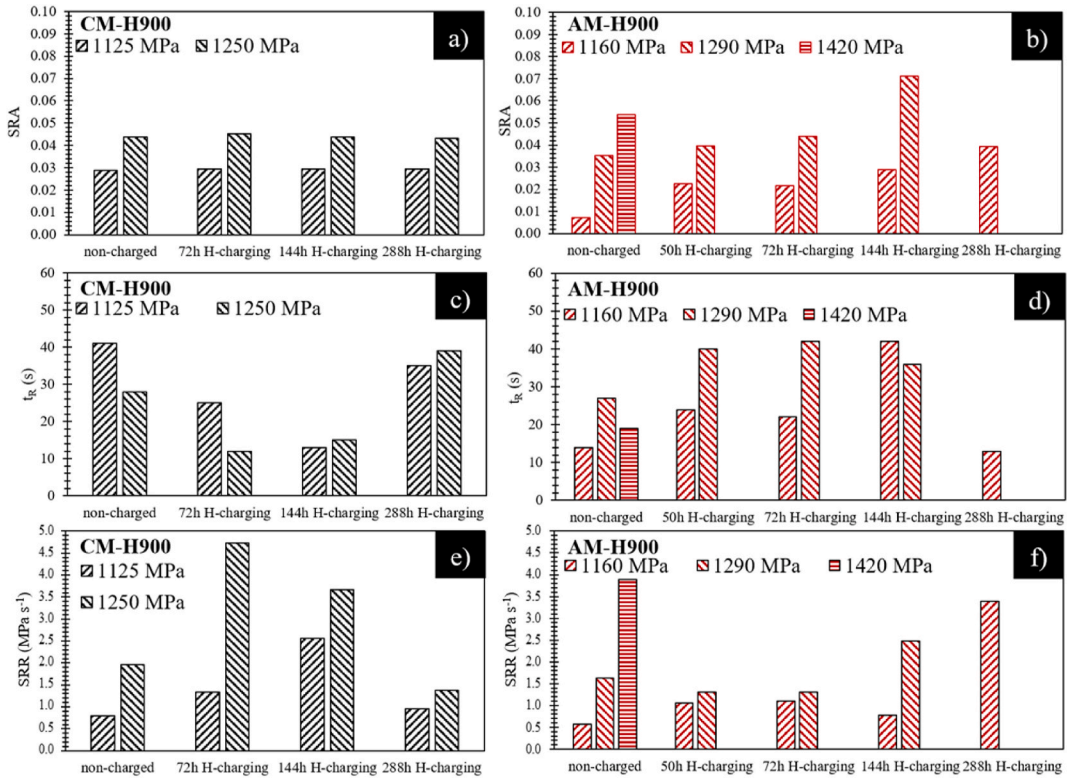

Fig. 9. Stress-relaxation ability (SRA) as calculated by Equation (2), critical time t_R as defined in Fig. 3 [21], and stress-relaxation rate (SRR) as given by Equation (3) for the (a, c, and e) CM and (b, d, and f) AM samples. The results are for the non-charged and hydrogen-charged samples at different hydrogen-charging durations and different initial relaxation stresses. (Color online only). (For interpretation of the references to colour in this figure legend, the reader is referred to the Web version of this article.)

two steps (Table 3). This could also be due to an increase in the dislocation mean free path for an almost constant mobile dislocation density.

Calculations of t_R values allowed a first approach for obtaining the SRR in the VRR regime (Fig. 9c and d) by considering the SRA values in parallel. A more detailed analysis was performed by calculating the SRR values (Fig. 9e and f), which showed a lower SRR for the AM samples. Finally, it should be noted that, for the AM samples, the stress-relaxation test was conducted until an initial stress level of 110% $YS_{0.2}$ (Figs. 8 and 9), which was not observed for the CM samples. This last finding showed that calculations of the SRA values, which were lower for the AM samples for a given initial stress level, were not sufficient to properly characterize the stress-relaxation ability.

Table 3
Plastic strain values evaluated from the tensile curves plotted after repetitive relaxation steps for both the CM and AM samples and for the non-charged and 144 h hydrogen-charged samples. Results are given for both the non-interrupted and interrupted stress-relaxation tests.

	Plastic strain ε_p (%)			
	CM-H900			
	80% $YS_{0.2}$	90% $YS_{0.2}$	100% $YS_{0.2}$	110% $YS_{0.2}$
non-charged	0.14	0.21	0.36	–
144 h H-charging	0.15	0.19	0.32	–
non-charged - interrupted	0.10	0.15	0.27	0.85
144 h H-charging - interrupted	0.17	0.21	0.39	1.70
	AM-H900			
	80% $YS_{0.2}$	90% $YS_{0.2}$	100% $YS_{0.2}$	110% $YS_{0.2}$
non-charged	0.09	0.10	0.20	0.48
144 h H-charging	0.08	0.10	0.35	–
non-charged - interrupted	0.04	0.06	0.17	–
144 h H-charging - interrupted	0.10	0.13	0.24	–

The difference in relaxation behavior between the AM and CM samples might be attributed to the differences in the amounts of reversed austenite, which is known to have both the capability to accommodate potential strain incompatibilities and to strain-harden. This might explain why the AM samples initially had a lower internal stress level, leading to a lower stress reduction during the first relaxation step (low SRA value for the test conducted at 90% $YS_{0.2}$). However, when the relaxation test was continued, i.e., with reloading until a higher initial stress level, the strain hardening of austenite led to an increase in the amount of internal stresses to be relaxed. This explains that for the tests carried out at 100% $YS_{0.2}$, the stress-relaxation amplitude of the AM samples increased and became close to that of the CM samples, as quantitatively shown by the SRA values (Fig. 9). Post-mortem energy-dispersive XRD analyses showed a TRIP effect component on the global behavior of the AM samples as in the tensile tests, because no austenite was detected on the fracture surfaces and only 1.5 ± 0.4% at 1.5 cm away from these surfaces. However, according to literature [26,38], the amount of reversed austenite gradually reduces during deformation. Such a decrease occurred for plastic strain levels definitively higher than those measured during these relaxation tests, which did not exceed 0.6% (Table 3). Therefore, the TRIP effect was assumed to have no significant effect on the mechanical behavior of the AM samples during the stress-relaxation tests. With this hypothesis, the capability to continue the stress-relaxation tests up to 110% $YS_{0.2}$ was attributed to the recovery of austenite owing to the relaxation of the internal stresses during the strain-holding steps.

Moreover, the nominal stress vs nominal strain curves without the strain-holding steps (i.e., tensile curves, as illustrated in Fig. 6) and with the strain-holding steps (i.e., obtained during the stress-relaxation tests)

were superimposed for both the CM and AM samples (Fig. 10). For both samples, the relaxation steps induced a slight decrease in the strain to fracture compared to monotonic loading, which was more pronounced for the CM samples. Furthermore, for the CM samples, strain localization occurred more rapidly following the relaxation tests compared to monotonic loading. However, the major result was that for the AM samples, the curve was significantly changed when strain-holding steps were interposed, with a progressive increase in the YS characteristic of incremental strain hardening during the successive reloading steps. This is in agreement with previous conclusions regarding the role of austenite in the mechanical behavior of AM samples. The influence of NbCs on the strain-hardening ability cannot be neglected considering the differences in the size of the precipitates between the AM and CM samples and their ability to pin the dislocations [5]. L-PBF materials often contain a much higher density of dislocations and other defects, which can affect the hydrogen content, and in turn change the mechanical properties. Here, STEM showed similar densities of dislocations in the initial H900 microstructures; therefore, this aspect was not addressed. The influence of pores cannot be disregarded, but it has a limited contribution owing to the low porosity.

The fracture surfaces observed at the end of the stress-relaxation tests (Fig. 11a and e) were similar to those observed during monotonic loading for both MSSs (Fig. 7a and e).

3.3.2. *Influence of hydrogen on the stress-relaxation curves*

Fig. 8 also shows the stress-relaxation curves plotted for both the CM and AM samples at 72, 144, and 288 h hydrogen-charging durations. Experiments were not performed for the 24 h hydrogen-charging duration because the amount of hydrogen was extremely low (Fig. 4a) to significantly influence the tensile properties of the MSSs (Fig. 6). For the AM samples, the stress-relaxation curves were also plotted for a 50 h hydrogen-charging duration, which led to an average hydrogen content (~8.1 ppm) similar to that measured for the 144 h hydrogen-charging duration (~7.2 ppm) of CM samples.

Hydrogen was found to have no influence on the stress-relaxation amplitude of the CM samples (Fig. 8a), which was corroborated by similar SRA values for both the non-charged and hydrogen-charged samples (Fig. 9a). Therefore, except for an increase in the SRR in the VRR regime when the hydrogen content increased (Fig. 9e), hydrogen had only a very minor effect on the global mechanical behavior of the CM samples, which is in agreement with the results of the tensile tests up to the occurrence of necking. Concerning the AM samples, the increase in hydrogen content led to a significant increase in the stress-relaxation amplitude, causing a significant decrease in the σ_∞ values for a given initial stress level (Fig. 8b). The stress reduction was significantly amplified with hydrogen, e.g., from 5 (40) MPa to 40 (100) MPa, which corresponded to SRA values of 0.007 (0.034) and 0.028 (0.07) (Fig. 9b), for the non-charged and 144 h hydrogen-charged samples, respectively, at an initial stress level of 90 (100) % $YS_{0.2}$. Moreover, the SRR in the VRR regime was found to increase as soon as the hydrogen content reached 8 ppm (50 h hydrogen charging) and then remained almost stable at higher hydrogen contents, for an initial stress level of 90% $YS_{0.2}$ (Fig. 9f).

Furthermore, for the 288 h hydrogen-charging duration, fracture of the AM specimens was observed during the strain-holding step corresponding to an initial stress level of 100% $YS_{0.2}$. SEM observations of the fracture surfaces after the relaxation tests showed that, for this hydrogen-charging duration (Fig. 11h), HE occurred and impeded the influence of hydrogen on the viscoplastic behavior of the sample to be observed. This result proved that for the AM samples, the 288 h

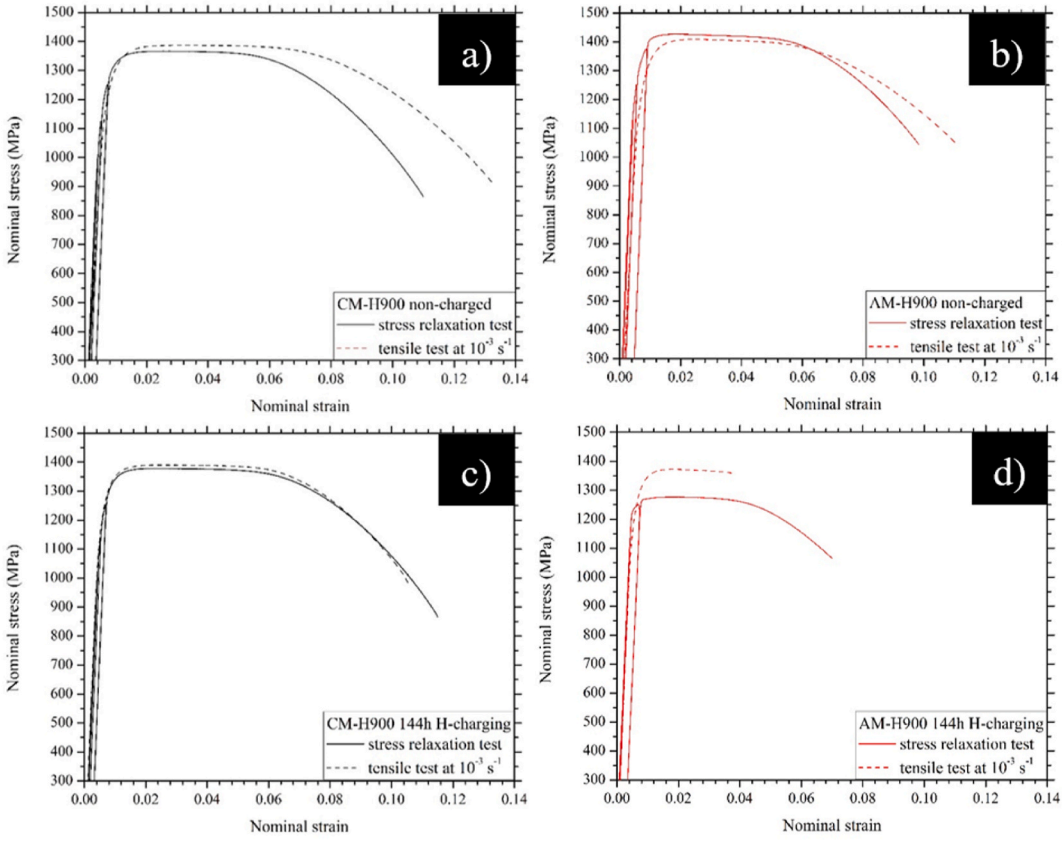

Fig. 10. Nominal stress vs nominal strain curves during tensile tests after repetitive relaxation steps for the (a and c) CM and (b and d) AM samples for both the non-charged and 144 h hydrogen-charged samples. The tensile curves commonly plotted with monotonic mechanical loading at the same loading rate (10^{-3} s^{-1}) are presented for comparison. (Color online only). (For interpretation of the references to colour in this figure legend, the reader is referred to the Web version of this article.)

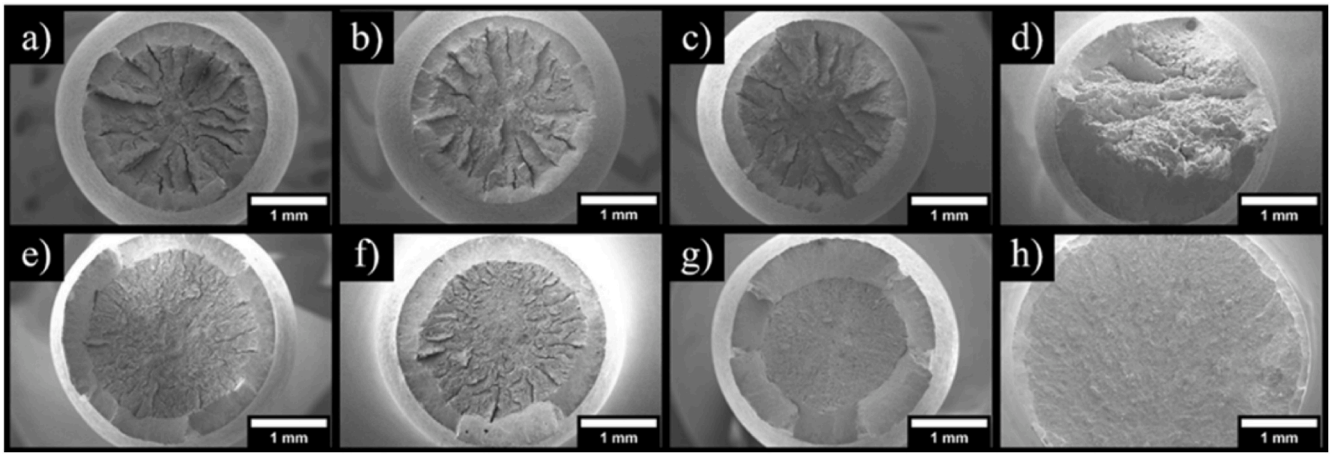

Fig. 11. SEM observations of fracture surfaces obtained after stress-relaxation tests for the (a–d) CM and (e–h) AM samples at different hydrogen-charging conditions: (a and e) uncharged, (b and f) 72 h, (c and g) 144 h, and (d and h) 288 h hydrogen charging. (Color online only).

hydrogen-charging duration was sufficient to reach the critical hydrogen content responsible for HE, whereas for the CM samples, this hydrogen content was not yet critical. This could be explained by referring to the influence of hydrogen on $YS_{0.2}$ values for the AM samples (Fig. 6). As the initial stress levels for the relaxation tests were based on the YS values for the non-charged samples, the 100% $YS_{0.2}$ initial stress was higher than the effective ultimate tensile strength for the hydrogen-charged samples.

The differences in the hydrogen sensitivity of both MSSs were in agreement with previous tensile test results (Fig. 6) and could not be explained only on the basis of the differences observed in the hydrogen amount for a given hydrogen-charging duration (Fig. 4). Indeed, for a similar hydrogen content (approximately 8 ppm for the 50 h and 144 h of hydrogen charging for the AM and CM samples, respectively), the hydrogen-charged AM samples showed a modified relaxation behavior compared to the non-charged samples, in contrast to the CM samples. These results clearly showed that the hydrogen-microstructure interactions were probably different between the two MSSs. Moreover, the influence of reversed austenite was strongly suspected because austenite is known as an efficient hydrogen trap [3,4,21,23,36]. The results suggested that hydrogen promoted the mobility of dislocations in the austenite for the AM samples, as shown in literature, for different steels [12,13,39–42] and demonstrated by the decrease in the activation volume due to hydrogen [32,43,44]. Oriani [39,40] showed such an effect for medium-carbon steel, referred to as the Lynch mechanism [45,46]. This was not the case for the CM samples, in which the amount of mobile dislocations was mainly controlled by the initial stress level. Nevertheless, the influence of NbCs and Cu-rich precipitates could not be neglected.

Comparison of the nominal stress vs nominal strain curves with and without the strain-holding steps for both the CM and AM samples, and for both the non-charged and 144 h hydrogen-charged samples (Fig. 10) corroborated the previous findings. For the CM samples, the curves plotted with and without the strain-holding steps were superimposed. For the 144 h hydrogen-charged AM samples, significant differences were observed between the two sets of curves. It was previously shown that for monotonic loading, hydrogen led to a decrease in the $YS_{0.2}$ and flow stress owing to the relaxation of internal stresses compared to that of the non-charged samples. When strain-holding steps were added to the hydrogen-charged samples, an additional decrease in the $YS_{0.2}$ and flow stress was observed. This strengthened our assumption concerning the influence of hydrogen on the mobility of dislocations in reversed austenite: the combined influence of hydrogen and loading/unloading steps led to a decrease in internal stresses due to strain accommodation. Consequently, necking became possible instead of promoting HE, as observed in the tensile tests. The fracture surfaces obtained after the relaxation steps confirmed the results (Fig. 11). Similar fracture surfaces were observed in both tensile tests and stress-relaxation tests for the CM samples, independent of the hydrogen content. In contrast, for the AM samples, the fracture surfaces after the stress-relaxation tests showed more noticeable necking for the 72 h hydrogen-charging duration (Fig. 11f) compared to that of the monotonic loading (Fig. 7g). Moreover, for the 144 h hydrogen-charging duration, necking was observed after the stress-relaxation tests (Fig. 11g), whereas no necking was observed after monotonic loading (Fig. 7h).

4. Discussion

Achieving similar and even better mechanical properties with AM processes often relies on obtaining microstructures similar to those of conventional processes. Concerning MSSs, in particular 17-4PH MSS, one major issue is the amount of reversed austenite obtained in the AM parts, which can vary over a large range and remain very often significantly higher than in CM samples [9,47,48]. The results described previously clearly showed that the non-charged AM 17-4PH MSS has a relaxation behavior that is significantly different from that of the non-charged CM MSS. The results highlighted the dual influence of austenite on the relaxation behavior of the AM 17-4PH MSS, i.e., a positive effect linked to its higher strain accommodation capability than martensitic phase, which competes with the negative effect due to its strain-hardening capability. When hydrogen was introduced inside the samples, it led to significant changes in the relaxation behavior of the AM samples. On the contrary, no significant changes were observed for the CM samples.

Our study thus highlighted that the relaxation behavior of the 17-4PH MSS in the presence of hydrogen was the result of very intricate couplings between the mechanical behavior of both austenite and martensite as well as specific interactions between hydrogen and both phases. To address this issue, additional interrupted stress-relaxation tests were performed. Indeed, as indicated in Fig. 5, hydrogen desorption occurred during the 168 h stress-holding step at 300 MPa, which allowed us to assess our conclusions regarding the influence of hydrogen on the specific mechanical behavior of austenite. Moreover, these tests allowed the investigation of the contribution of static aging of the martensitic deformation structure.

Fig. 12 depicts the results of the interrupted stress-relaxation tests for both the non-charged and 144 h hydrogen-charged AM and CM samples. The results obtained for the non-interrupted stress-relaxation tests are indicated for comparison. For the non-charged CM samples, the stress-relaxation amplitude slightly decreased for the interrupted tests

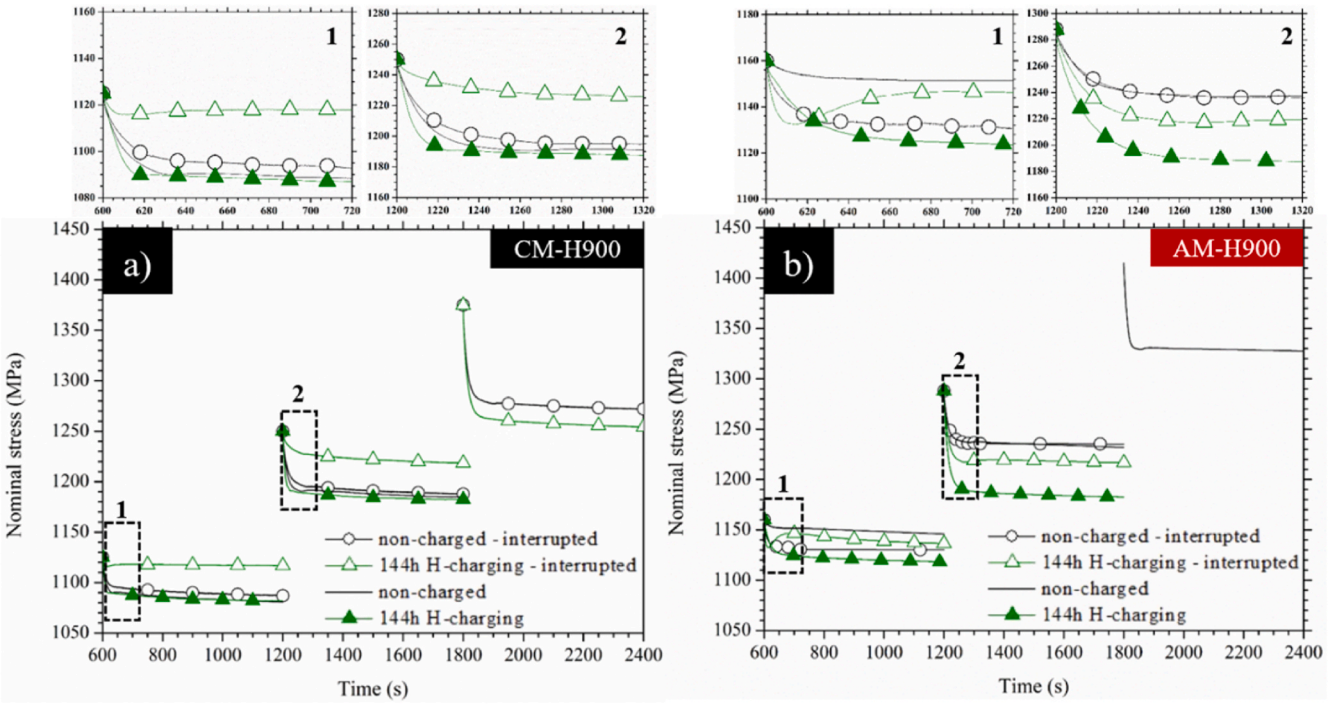

Fig. 12. Stress-relaxation curves in the nominal stress vs time representation for the a) CM and b) AM samples for both the non-charged and 144 h hydrogen-charged samples. Results are given for both the non-interrupted and interrupted tests (stress-holding step at 300 MPa for 168 h). Inserts indicate zoomed views of the first 120 s of the relaxation steps. (Color online only). (For interpretation of the references to colour in this figure legend, the reader is referred to the Web version of this article.)

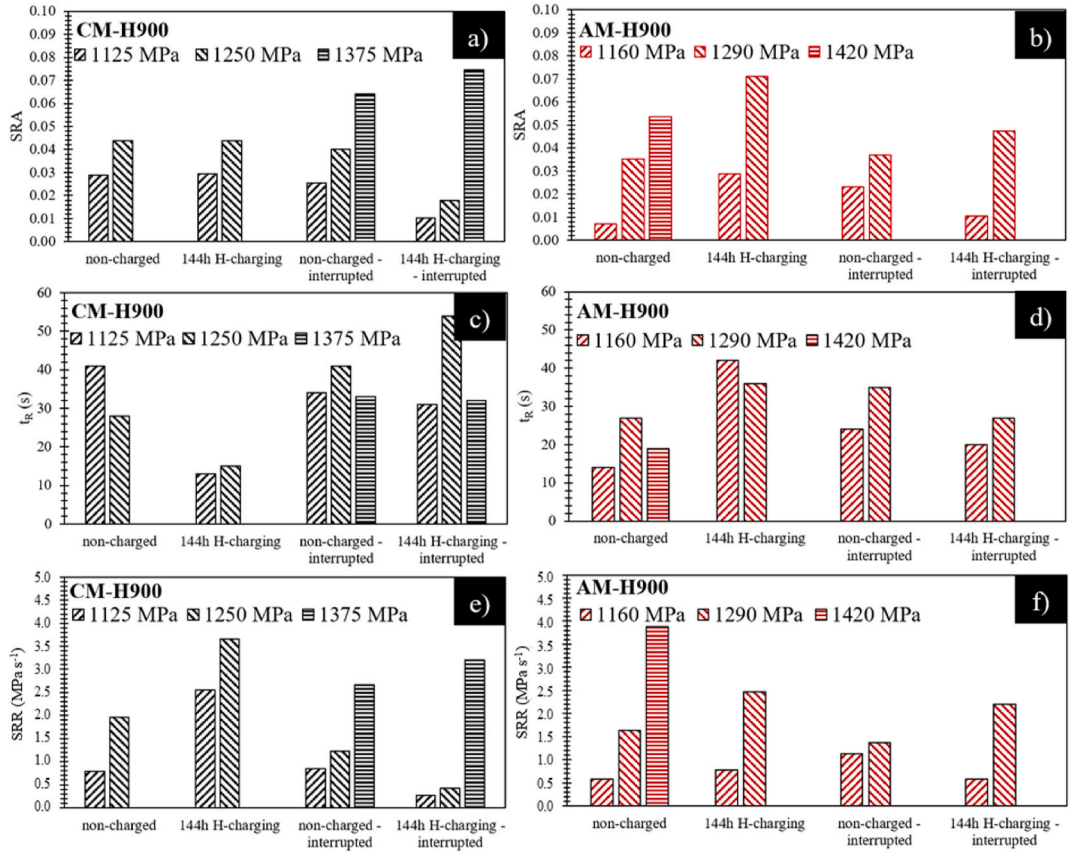

Fig. 13. SRA as calculated by Equation (2), critical time t_R as defined in Fig. 3 [21], and SRR as given by Equation (3), for the (a, c, and e) CM and (b, d, and f) AM samples. Results are for the non-charged and 144 h hydrogen-charged samples, for both the non-interrupted and interrupted tests (stress-holding step at 300 MPa for 168 h). (Color online only). (For interpretation of the references to colour in this figure legend, the reader is referred to the Web version of this article.)

compared to the non-interrupted ones. Moreover, it was possible to perform the interrupted tests until an initial stress level of 110% $YS_{0.2}$, whereas specimen fracture occurred before reaching this stress level for the non-interrupted tests. This highlighted the positive effect of static aging of the martensitic deformation structures occurring during the stress-holding step at 300 MPa, allowing subsequent deformation. For the 144 h hydrogen-charged CM samples, a similar behavior was observed. However, the decrease in the stress-relaxation amplitude of the interrupted tests compared to the non-interrupted ones was more pronounced than for the non-charged samples, at initial stress levels of 90 and 100% $YS_{0.2}$, as shown by a larger decrease in the SRA values (Fig. 13). This led to SRA values significantly lower for the 144 h hydrogen-charged samples compared to the non-charged samples for the interrupted tests, whereas no influence of hydrogen was observed for the non-interrupted tests. As hydrogen had no influence on mobile dislocations for the CM samples, as exhibited by the non-interrupted tests, these results clearly showed that hydrogen significantly influenced the static aging of martensite, which could be attributed to the effect of hydrogen on the pinning of dislocations by interstitials and/or the influence of hydrogen on the recovery of dislocation substructures in martensite. For higher stress levels (110% $YS_{0.2}$), the SRA evolution was inverted, with SRA values of the 144 h hydrogen-charged samples higher than those of the non-charged samples, for the interrupted tests (Fig. 13). The strain hardening associated with the initial stress level increment should hinder the effects of hydrogen on the static aging of martensite. Furthermore, the hydrogen content measured after the 168 h stress-holding step at 300 MPa was only 2.3 ppm (2.8 ppm) for the 144 h hydrogen-charged CM samples (AM samples). Measurements performed at the end of the interrupted stress-relaxation tests led to a hydrogen content of 2.1 ppm (2.2 ppm) for the CM (AM) samples. Therefore, the stress-holding stage at 300 MPa was associated with strong hydrogen desorption; however, during the incremental relaxation tests, the hydrogen content should also decrease gradually. This could explain the inversion in the SRA evolution at an initial stress level of 110% $YS_{0.2}$. Nevertheless, the hydrogen contents corresponded to the mean values, and at a local scale, the hydrogen content was assumed to remain high enough to influence the different processes described previously. Finally, it is interesting to note that the density of mobile dislocations should evolve during hydrogen desorption in relation to vacancy concentration [49]; however, this point was not investigated here.

For the non-charged AM samples, the results were significantly different from those of the non-charged CM samples (Fig. 12). Indeed, for the interrupted stress-relaxation tests, the stress-relaxation amplitude was increased at an initial stress level of 90% $YS_{0.2}$ and unchanged at 100% $YS_{0.2}$, as exhibited by the SRA values (Fig. 13). Moreover, the tests could not be conducted until 110% $YS_{0.2}$, contrary to the non-interrupted tests. These results suggested that martensite static aging was not efficient for the AM samples. This should be related to the austenite to martensite ratio with impoverishment of martensite in interstitial elements, which segregated in austenite. In addition, this was clearly related to the distribution of reversed austenite in the martensitic matrix with interlath reversed austenite [14,16]. Furthermore, austenite static aging, leading to a reduced capability to accommodate strain incompatibilities, must be taken into account. For the 144 h hydrogen-charged samples, the stress-relaxation amplitude (Fig. 12), and therefore, the SRA values (Fig. 13), decreased for the interrupted tests compared to the non-interrupted ones. Such a result could be related to hydrogen desorption during the stress-holding step at 300 MPa, as quantified above, so that hydrogen could no longer significantly affect the dislocation mobility [27–32]. However, Fig. 13 shows that the SRA values of the 144 h hydrogen-charged samples after interrupted tests are slightly higher than those of the non-charged samples after non-interrupted tests. This confirmed, as previously suggested, that despite the strong desorption of hydrogen during the 168 h stress-holding step, a non-negligible amount of hydrogen remained in the sample, at least at a local scale, during the incremental stress-relaxation tests. Therefore, the remaining hydrogen still had an effect on the dislocation mobility [32,43,44]. Groh [50] and Martin [51] showed that the relaxation properties of ferritic steels were linked to the mobility of both edge and screw dislocations based on two different mechanisms. However, investigating the influence of hydrogen on the two proposed mechanisms is beyond the scope of the present study. Finally, the relaxation behavior of the AM samples during the interrupted stress-relaxation tests should also be explained by considering that hydrogen could affect martensite static aging for the AM samples, but to a lesser extent than for the CM samples. As indicated in the non-charged AM samples, austenite static aging should also be considered.

5. Conclusion

The major conclusions of the study are summarized as follows:

1. Substantial differences in relaxation properties were observed between the non-charged CM and AM 17-4PH MSSs in the H900 state. These differences were attributed to the higher reversed austenite amount in the AM MSS (12%) than that in the CM MSS (0.8%), which was identified as a key parameter, even though other microstructural features differed between both MSSs. With a low austenite amount, the relaxation properties at room temperature of the CM MSS were mainly controlled by martensitic static aging, insofar as this phenomenon could occur. For the AM MSS, austenite significantly modified its mechanical behavior during relaxation. The dual role of austenite, namely, a positive effect favoring plastic deformation of the 17-4PH steel owing to the larger strain accommodation capability of austenite compared to martensite and a negative effect due to the strain-hardening capability of austenite, must be considered. Furthermore, when a stress-holding stage was added to the incremental stress-relaxation tests, another detrimental effect of austenite was observed. Martensite static aging was strongly reduced owing to martensite depletion in interstitial elements because they concentrate in austenite.
2. A completely different relaxation behavior was observed for the hydrogen-charged AM and CM samples, which suggested significant differences in the susceptibility to HE between both MSSs. For the CM MSS with a low austenite amount, hydrogen influenced the martensite static aging so that the relaxation behavior could be modified insofar as in-service conditions allow static aging to occur. No other significant influence of hydrogen was observed. However, for the high-austenite 17-4PH AM MSS, hydrogen could increase the mobility of dislocations in austenite because of the reduction in their activation volume in the presence of hydrogen.

The results are of great interest when they are considered in the framework for the development of additive manufacturing processes. They showed that regulating the reversed austenite amount, and therefore regulating the process parameters, is required to control the relaxation properties of MSSs and their susceptibility to HE. They provided a new insight into the relaxation properties of 17-4PH MSS and future development of additive manufacturing processes, namely, it is necessary to adjust the austenite amount to take advantage of the coupling between viscoplasticity and hydrogen for improving the in-service behavior of structures via stress relaxation.

CRediT authorship contribution statement

N. Guennouni: Investigation, Formal analysis, Validation, Visualization, Methodology, Data curation, Writing – review & editing. **D. Maisonnette:** Funding acquisition, (financial support), Resources (Materials), Project administration, Supervision, Writing – review & editing. **C. Grosjean:** Funding acquisition, (financial support), Resources (Materials), Project administration, Supervision, Writing – review & editing.

E. Andrieu: Conceptualization, Formal analysis, Methodology, Validation, Writing – review & editing. **D. Poquillon:** Conceptualization, Formal analysis, Methodology, Validation, Visualization, Supervision, Data curation, Writing – review & editing. **C. Blanc:** Funding acquisition, Methodology, Formal analysis, Project administration, Supervision, Validation, Conceptualization, Data curation, Writing – original draft, Writing – review & editing.

Declaration of competing interest

The authors declare that they have no known competing financial interests or personal relationships that could have appeared to influence the work reported in this paper.

Acknowledgments

The authors thank the ANRT for their financial support (Nizar Guennouni's PhD thesis).

Appendix A. Supplementary data

Supplementary data to this article can be found online at https://doi.org/10.1016/j.msea.2021.142125.

Data availability

The raw/processed data required to reproduce these findings cannot be shared at this time, as the data also form part of an ongoing study.

References

[1] M.B. Djukic, G.M. Bakic, V.S. Zeravcic, A. Sedmak, B. Rajicic, Hydrogen embrittlement of industrial components: prediction, prevention, and models, Corrosion 72 (2016) 943–961, https://doi.org/10.5006/1958.
[2] M.L. Martin, M. Dadfarnia, A. Nagao, S. Wang, P. Sofronis, Enumeration of the hydrogen-enhanced localized plasticity mechanism for hydrogen embrittlement in structural materials, Acta Mater. 165 (2019) 734–750, https://doi.org/10.1016/j.actamat.2018.12.014.
[3] K.G. Solheim, J.K. Solberg, J. Walmsley, F. Rosenqvist, T.H. Bjørnå, The role of retained austenite in hydrogen embrittlement of supermartensitic stainless steel, Eng. Fail. Anal. 34 (2013) 140–149, https://doi.org/10.1016/j.engfailanal.2013.07.025.
[4] Z. Yang, Z. Liu, J. Liang, J. Su, Z. Yang, B. Zhang, G. Sheng, Correlation between the microstructure and hydrogen embrittlement resistance in a precipitation-hardened martensitic stainless steel, Corrosion Sci. 182 (2021) 109260, https://doi.org/10.1016/j.corsci.2021.109260.
[5] S. Zhang, J. Wan, Q. Zhao, J. Liu, F. Huang, Y. Huang, X. Li, Dual role of nanosized NbC precipitates in hydrogen embrittlement susceptibility of lath martensitic steel, Corrosion Sci. 164 (2020) 108345, https://doi.org/10.1016/j.corsci.2019.108345.
[6] A. Nagao, M. Dadfarnia, B.P. Somerday, P. Sofronis, R.O. Ritchie, Hydrogen-enhanced-plasticity mediated decohesion for hydrogen-induced intergranular and "quasi-cleavage" fracture of lath martensitic steels, J. Mech. Phys. Solid. 112 (2018) 403–430, https://doi.org/10.1016/j.jmps.2017.12.016.
[7] M. Alnajjar, F. Christien, C. Bosch, K. Wolski, A comparative study of microstructure and hydrogen embrittlement of selective laser melted and wrought 17–4 PH stainless steel, Mater. Sci. Eng. 785 (2020) 139363, https://doi.org/10.1016/j.msea.2020.139363.
[8] J.-G. Sezgin, J. Yamabe, Tensile and fatigue properties of 17-4PH martensitic stainless steels in presence of hydrogen, Proc. Struct. Integ. 19 (2019) 249–258, https://doi.org/10.1016/j.prostr.2019.12.027.
[9] Y. Sun, R.J. Hebert, M. Aindow, Effect of heat treatments on microstructural evolution of additively manufactured and wrought 17-4PH stainless steel, Mater. Des. 156 (2018) 429–440, https://doi.org/10.1016/j.matdes.2018.07.015.
[10] Y. Sun, R.-J. Hebert, M. Aindow, Effect of laser scan length on the microstructure of additively manufactured 17-4PH stainless steel thin-walled parts, Addit. Manuf. 35 (2020) 101302, https://doi.org/10.1016/j.addma.2020.101302.
[11] S. Pasebani, M. Ghayoor, S. Badwe, H. Irrinki, S.-V. Atre, Effects of atomizing media and post processing on mechanical properties of 17-4 PH stainless steel manufactured via selective laser melting, Addit. Manuf. 22 (2018) 127–137, https://doi.org/10.1016/j.addma.2018.05.011.
[12] I.M. Robertson, The effect of hydrogen on dislocation dynamics, Eng. Fract. Mech. 64 (1999) 649–673, https://doi.org/10.1016/S0013-7944(99)00094-6.
[13] Y. Ogawa, H. Hosoi, K. Tsuzaki, T. Redarce, O. Takakuwa, H. Matsunaga, Hydrogen, as an alloying element, enables a greater strength-ductility balance in an Fe-Cr-Ni-based, stable austenitic stainless steel, Acta Mater. 199 (2020) 181–192, https://doi.org/10.1016/j.actamat.2020.08.024.
[14] A. Barroux, N. Ducommun, E. Nivet, L. Laffont, C. Blanc, Pitting corrosion of 17-4PH stainless steel manufactured by laser beam melting, Corrosion Sci. 169 (2020) 108594, https://doi.org/10.1016/j.corsci.2020.108594.
[15] A. Barroux, T. Duguet, N. Ducommun, E. Nivet, J. Delgado, L. Laffont, C. Blanc, Combined XPS/TEM study of the chemical composition and structure of the passive film formed on additive manufactured 17-4PH stainless steel, Surf. Interf. 22 (2021) 100874, https://doi.org/10.1016/j.surfin.2020.100874.
[16] N. Guennouni, A. Barroux, C. Grosjean, D. Maisonnette, E. Nivet, E. Andrieu, D. Poquillon, L. Laffont, C. Blanc, Comparative study of the microstructure between a laser beam melted 17-4PH stainless steel and its conventional counterpart, Mater. Sci. Eng. 823 (2021) 141718, https://doi.org/10.1016/j.msea.2021.141718.
[17] C.E.A. Cast3M. http://www-cast3m.cea.fr/, 2020.
[18] S.L.I. Chan, H.L. Lee, J.R. Yang, Effect of retained austenite on the hydrogen content and effective diffusivity of martensitic structure, Metall. Mater. Trans. 22 (1991) 2579–2586, https://doi.org/10.1007/BF02851351.
[19] P. Ferrin, S. Kandoi, A.U. Nilekar, M. Mavrikakis, Hydrogen adsorption, absorption and diffusion on and in transition metal surfaces: a DFT study, Surf. Sci. 606 (2012) 679–689, https://doi.org/10.1016/j.susc.2011.12.017.
[20] B. Ladna, H.K. Birnbaum, A study of hydrogen transport during plastic deformation, Acta Metall. 35 (1987) 1775–1778, https://doi.org/10.1016/0001-6160(87)90123-4.
[21] Z. Hua, D. Wang, Z. Liu, Y. Zhang, S. Zhu, Hydrogen distribution at twin boundary in austenitic stainless steel studied by scanning Kelvin probe force microscopy, Mater. Lett. 234 (2019) 175–178, https://doi.org/10.1016/j.matlet.2018.09.087.
[22] Y. Yang, L. Zhan, C. Liu, X. Wang, Q. Wang, Z. Tang, G. Li, M. Huang, Z. Hu, Stress-relaxation ageing behavior and microstructural evolution under varying initial stresses in an Al–Cu alloy: experiments and modeling, Int. J. Plast. 127 (2020) 102646, https://doi.org/10.1016/j.ijplas.2019.102646.
[23] Y. Zhang, W. Hui, X. Zhao, C. Wang, W. Cao, H. Dong, Effect of reverted austenite fraction on hydrogen embrittlement of TRIP-aided medium Mn steel (0.1C-5Mn), Eng. Fail. Anal. 97 (2019) 605–616, https://doi.org/10.1016/j.engfailanal.2019.01.018.
[24] J. Yoo, M.C. Jo, D.W. Kim, H. Song, M. Koo, S.S. Sohn, S. Lee, Effects of Cu addition on resistance to hydrogen embrittlement in 1 GPa-grade duplex lightweight steels, Acta Mater. 196 (2020) 370–383, https://doi.org/10.1016/j.actamat.2020.06.051.
[25] C. Rousseau, A. Oudriss, R. Milet, X. Feaugas, M. El May, N. Saintier, Q. Tonizzo, M. Msakni-Malouche, Effect of aging treatment on apparent hydrogen solubility and trapping in a new generation maraging steel, Scripta Mater. 183 (2020) 144–148, https://doi.org/10.1016/j.scriptamat.2020.03.013.
[26] M.-M. Wang, C.C. Tasan, D. Ponge, D. Raabe, Spectral TRIP enables ductile 1.1 GPa martensite, Acta Mater. 111 (2016) 262–272, https://doi.org/10.1016/j.actamat.2016.03.070.
[27] H.K. Birnbaum, P. Sofronis, Hydrogen-enhanced localized plasticity—a mechanism for hydrogen-related fracture, Mater. Sci. Eng. 176 (1994) 191–202, https://doi.org/10.1016/0921-5093(94)90975-X.
[28] S.-P. Lynch, Environmentally assisted cracking: overview of evidence for an adsorption-induced localised-slip process, Acta Metall. 36 (1988) 2639–2661.
[29] D. Guedes, L. Cupertino Malheiros, A. Oudriss, S. Cohendoz, J. Bouhattate, J. Creus, F. Thebault, M. Piette, X. Feaugas, The role of plasticity and hydrogen flux in the fracture of a tempered martensitic steel: a new design of mechanical test until fracture to separate the influence of mobile from deeply trapped hydrogen, Acta Mater. 186 (2020) 133–148, https://doi.org/10.1016/j.actamat.2019.12.045.
[30] R. Kirchheim, Revisiting hydrogen embrittlement models and hydrogen-induced homogeneous nucleation of dislocations, Scripta Mater. 62 (2010) 67–70, https://doi.org/10.1016/j.scriptamat.2009.09.037.
[31] J.P. Hirth, Effects of hydrogen on the properties of iron and steel, Metall. Trans. A. 11 (1980) 861–890, https://doi.org/10.1007/BF02654700.
[32] S. Yuan, Y. Zhu, M. Huang, S. Liang, Z. Li, Dislocation-density based crystal plasticity model with hydrogen-enhanced localized plasticity in polycrystalline face-centered cubic metals, Mech. Mater. 148 (2020) 103472, https://doi.org/10.1016/j.mechmat.2020.103472.
[33] H. Kamei, Y. Matsumoto, H. Suzuki, K. Takai, Change in dislocation mobility of tempered martensitic steel through charged hydrogen, IOP Conf. Ser. Mater. Sci. Eng. 461 (2018), 012034, https://doi.org/10.1088/1757-899X/461/1/012034.
[34] D. Wang, X. Lu, D. Wan, Z. Li, A. Barnoush, In-situ observation of martensitic transformation in an interstitial metastable high-entropy alloy during cathodic hydrogen charging, Scripta Mater. 173 (2019) 56–60, https://doi.org/10.1016/j.scriptamat.2019.07.042.
[35] G.G. Maksimovich, I. Yu Tretyak, L.M. Ivas'kevich, T.V. Slipchenko, Role of the martensite transformation in hydrogen embrittlement of unstable austenitic steels, Mater. Sci. 21 (1986) 320–323, https://doi.org/10.1007/BF0072655.
[36] Y.H. Fan, B. Zhang, H.L. Yi, G.S. Hao, Y.Y. Sun, J.Q. Wang, E.H. Han, W. Ke, The role of reversed austenite in hydrogen embrittlement fracture of S41500 martensitic stainless steel, Acta Mater. 139 (2017) 188–195, https://doi.org/10.1016/j.actamat.2017.08.011.
[37] N.-V. Nguyen, Q.-A. Vu, S.-E. Kim, An experimental study on stress relaxation behaviour of high strength steel wire: microstructural evolution and degradation of mechanical properties, Construct. Build. Mater. 261 (2020) 119926, https://doi.org/10.1016/j.conbuildmat.2020.119926.
[38] D. Raabe, D. Ponge, O. Dmitrieva, B. Sander, Nanoprecipitate-hardened 1.5 GPa steels with unexpected high ductility, Scripta Mater. 60 (2009) 1141–1144, https://doi.org/10.1016/j.scriptamat.2009.02.062.
[39] R.-A. Oriani, P.-H. Josephic, Hydrogen-enhanced load relaxation in a deformed medium carbon steel, Acta Metall. 27 (1979) 997–1005.
[40] R.-A. Oriani, Hydrogen-the versatile embrittler, Corrosion 43 (1987) 390–397.

[41] D.-P. Abraham, C.-J. Altstetter, Hydrogen-enhanced localization of plasticity in an austenitic stainless steel, Metall. Mater. Trans. 26A (1995) 2859–2871, https://doi.org/10.1007/BF02669644.
[42] A. Varma, H. Krishnaswamy, J. Jain, M.-G. Lee, F. Barlat, Advanced constitutive model for repeated stress relaxation accounting fortransient mobile dislocation density and internal stress, Mech. Mater. 133 (2019) 138–153, https://doi.org/10.1016/j.mechmat.2019.03.009.
[43] S. Wang, N. Hashimoto, S. Ohnuki, Effects of hydrogen on activation volume and density of mobile dislocations in iron-based alloy, Mater. Sci. Eng. 562 (2013) 101–108, https://doi.org/10.1016/j.msea.2012.10.100.
[44] S. Wang, M.L. Martin, P. Sofronis, S. Ohnuki, N. Hashimoto, I.M. Robertson, Hydrogen-induced intergranular failure of iron, Acta Mater. 69 (2014) 275–282, https://doi.org/10.1016/j.actamat.2014.01.060.
[45] S.-P. Lynch, Hydrogen embrittlement and liquid-metal embrittlement in nickel single crystals, Scripta Metall. 13 (1979) 1051–1056.
[46] S.-P. Lynch, A fractographic study of hydrogen-assisted cracking and liquid-metal embrittlement in nickel, J. Mater. Sci. 21 (1986) 692–704.
[47] L. Facchini, N. Vicente, I. Lonardelli, E. Magalini, P. Robotti, A. Molinari, Metastable Austenite in 17–4 precipitation-hardening stainless steel produced by selective laser melting, Adv. Eng. Mater. 12 (2010) 184–188, https://doi.org/10.1002/adem.200900259.
[48] T. LeBrun, T. Nakamoto, K. Horikawa, H. Kobayashi, Effect of retained austenite on subsequent thermal processing and resultant mechanical properties of selective laser melted 17–4 PH stainless steel, Mater. Des. 81 (2015) 44–53, https://doi.org/10.1016/j.matdes.2015.05.026.
[49] S. Li, Y. Li, Y.-C. Lo, T. Neeraj, R. Srinivasan, X. Ding, J. Sun, L. Qi, P. Gumbsch, J. Li, The interaction of dislocations and hydrogen-vacancy complexes and its importance for deformation-induced proto nano-voids formation in α-Fe, Int. J. Plast. 74 (2015) 175–191, https://doi.org/10.1016/j.ijplas.2015.05.017.
[50] P. Groh, R. Conte, Stress relaxation and creep in α-iron filamentary single crystals at low temperature, Acta Metall. 19 (1971) 895–902, https://doi.org/10.1016/0001-6160(71)90082-4.
[51] J.L. Martin, T. Kruml, Characterizing thermally activated dislocation mobility, J. Alloys Compd. 378 (2004) 2–12, https://doi.org/10.1016/j.jallcom.2003.10.063.